Journal of Membrane Science 758 (2026) 126018

Contents lists available at ScienceDirect

Journal of Membrane Science

journal homepage: www.elsevier.com/locate/memsci

Adhesion behavior of polydimethylsiloxane with porous membranes

Meril Moni [a], Emma Letourneau [a], Sundus Imtiaz Qureshi [a,b], Christina Carbrello [c], Jason Killgore [d], Yifu Ding [a,*]

[a] Membrane Applications Science, and Technology (MAST) Center, Paul M. Rady Department of Mechanical Engineering, University of Colorado Boulder, Boulder, CO, 80309, USA
[b] Center for Interdisciplinary Research in Basic Sciences (SA-CIRBS), International Islamic University, Islamabad, 44000, Pakistan
[c] EMD Millipore Corporation, an affiliate of Merck, Bedford, MA, 01730, USA[1]
[d] Applied Chemicals and Materials Division, National Institute of Standards and Technology, Boulder, CO, 80305, USA

ARTICLE INFO

Keywords:
Porous membrane
PDMS
Adhesion
Mechanical interlocking

ABSTRACT

Multilayer architecture is widely employed in membrane technologies. Among them, polydimethylsiloxane (PDMS) films are often laminated onto porous supports to either serve as selective layers for pervaporation or as gutter layers for gas separation. However, the interfacial properties governing adhesion between PDMS and porous supports remain poorly understood. Here, we examine the adhesion between PDMS and symmetric polyvinylidene fluoride (PVDF) membranes as well as asymmetric polyethersulfone (PES) membranes. Compared with bulk PVDF and PES films, the PDMS-infiltrated membranes exhibit interfacial fracture toughness (G_c) values that are 3–25 times higher, attributed to mechanical interlocking. The G_c value increases with increasing pore size and porosity of the membranes. Analysis using the Gent model suggests that the fracture depth of the infiltrated PDMS is approximately 100 -200 nm for membranes with pore sizes below 100 nm, and 1 -2 μm for membranes with pore sizes above 200 nm. These findings provide fundamental insights into adhesion mechanisms in multilayer membrane systems and offer design guidelines for improving the mechanical integrity of composite membranes.

1. Introduction

Membrane-based separation technologies are versatile and energy efficient. Multilayer configurations are commonly employed in many applications [1,2]. Polydimethylsiloxane (PDMS), one of the most permeable polymers, can be directly laminated onto porous supports, as in pervaporation membranes [3,4], membrane bioreactors [5], gas separation membranes [6–8], and even desalination membranes [9]. PDMS is also versatile and can be further modified to enhance separation performance [10] or other surface/interfacial characteristics [11]. The interfacial properties between PDMS and porous supports, particularly adhesion, are important for the performance and reliability of these membrane technologies [12]. However, quantitative studies of the adhesion between PDMS and porous membranes remain limited [12,13].

In a broader sense, the adhesion between porous membranes and polymer films remains poorly understood. Recently, the adhesion between asymmetric polyethersulfone (PES) membranes and a polypropylene (PP) substrate, often used in microfiltration devices, was systematically investigated [14–17]. Given their low surface energies, intrinsic (thermodynamic) adhesion between the PES membranes and PP is low. Consequently, mechanical interlocking from infiltrated PP in the membrane pores, driven by capillary pressure [15,16] or hydraulic pressure [17], is necessary for achieving strong interfacial fracture toughness. However, achieving effective pore infiltration can be difficult during high-throughput manufacturing, especially for membranes with small pore sizes and low surface porosities [17]. For these membranes, enhanced chemical interactions using plasma treatment can improve the adhesion strength, even with limited polymer infiltration [14].

Beyond the aforementioned studies, a few studies have probed adhesion between PDMS and porous supports using AFM-based indentation/scratch tests [12,13]. However, such tests do not provide quantitative values of adhesion strength or detailed failure mechanisms. In this study, we systematically quantify the adhesion strength between PDMS and porous membranes using peel tests. Both symmetric PVDF membranes and asymmetric PES membranes were examined. The effects

* Corresponding author.
E-mail address: yifu.ding@colorado.edu (Y. Ding).
[1] The Life Science Business of Merck Operates As MilliporeSigma in the U.S. and Canada.

https://doi.org/10.1016/j.memsci.2026.126018
Received 1 June 2026; Received in revised form 6 August 2026; Accepted 7 August 2026
Available online 10 August 2026

of membrane chemistry, pore size, and debonding strain rate on the adhesion strength of the PDMS-infiltrated membranes were quantified. The observed interfacial fracture toughness is analyzed using the classical Gent model developed for pulling elastomers out of cylindrical pores. Most importantly, a fracture depth of PDMS associated with the mechanical interlocking is estimated, which is important for designing PDMS/porous supports that simultaneously achieve robust adhesion and optimal membrane performance.

2. Materials and methods

2.1. Materials

Two symmetric PVDF membranes (V-100 and V-650) and four asymmetric PES membranes were fabricated by Merck using a standard phase inversion process. The V-100 and V-650 membranes correspond to the commercial "VVPP" and "DVPP" membranes, which have been chemically modified to be hydrophilic. The four PES membranes (denoted as "S") contain two different surface chemistries ("U" for unmodified and "M" for acrylamide-modified), each with two different nominal pore sizes (200 nm and 20 nm), which are referred to as S-U200, S-M200, S-U20 and S-M20, respectively. The acrylamide modification results in a slight decrease in water contact angle, e.g. from 66.5 ± 3.7° for S-U200 to 60.8 ± 3.3° for S-M200. The PDMS used was Sylgard 184 with a base-to-curing-agent ratio of 10:1.

2.2. Mechanical properties of PDMS

Mechanical properties of the cured PDMS films were characterized by static tensile testing using an Instron (5965, 50 N load cell) at room temperature under five different strain rates: 10, 50, 200, 500, and 2000 %/min. At each strain rate, the sample was stretched until failure, and the resulting stress-strain curve was used to estimate the tensile fracture toughness of the PDMS at the corresponding strain rate. The loss modulus (E'') of the PDMS as a function of frequency (0.01 - 200 Hz) at room temperature was measured using dynamic mechanical analysis (DMA, TA Instruments, Q800). A strain amplitude of 0.1 % was used to ensure a linear mechanical response.

2.3. Adhesion sample preparation and testing

A PDMS precursor (10: 1 ratio, total mass, 2.5 g) was manually mixed for 2 min, degassed under vacuum for 1 h, and then poured on top of a membrane sample. A 1-mm spacer was used to control the PDMS thickness above the membrane, and the pore-wetting time was approximately 30 min. At this thickness (1 mm), cohesive failure of PDMS did not occur during the peel test, enabling us to quantify the interfacial debonding between PDMS and the membranes. For all four asymmetric PES membranes, the tight-pore side was in direct contact with the PDMS. The PDMS precursors quickly wetted the membrane pores due to their low surface energy and viscosity (3.5 $Pa{\cdot}\,s$, according to the manufacturer specification) [15,16], as illustrated in Fig. 1. Complete pore wetting by PDMS was evidenced by a change in membrane appearance from white to nearly transparent. The PDMS-infiltrated membrane sample was cured at 150 °C for 1 h and then cut into 40 mm × 12 mm specimens for the peel tests.

Both dense PVDF and PES films were prepared as control samples to examine the impact of pores on adhesion behavior. The films were prepared by uniaxial compression using a thermal press at 180 °C for PVDF (T_m = 155 °C) and 260 °C for PES (T_g = 200 °C) with a pressure of approximately 50 MPa for 5 min [18]. Using the same procedures as described above, PDMS/PES film and PDMS/PVDF film bilayers were prepared. Lastly, pre-cured PDMS/dense PVDF and pre-cured PDMS/dense PES bilayers were prepared by laminating the pre-cured PDMS films onto the dense PVDF and PES films. However, their adhesion strength could not be quantified because the bilayers separated upon loading.

The adhesion between PDMS and the membranes (or dense films) was quantified using a T-peel test (ASTM D1876) performed on an Instron 5965 universal testing machine (50 N load cell) with peel strain rates from 10 %/min to 2000 %/min. For each sample, the PDMS layer was manually separated from the membrane to create unbonded regions that served as grips during tensile testing. For each system, four replicates were tested. All tests were conducted at room temperature.

2.4. Imaging and spectroscopic measurements

SEM (Thermo Fisher Apreo, Volumescope, 1,129,194) was used to characterize the morphology of both virgin membranes and the PDMS-infiltrated membranes. Cross sections of the membranes used for SEM imaging were obtained by fracturing in liquid nitrogen. A 2-nm platinum coating was deposited on each sample to mitigate charging effects. AFM (Cypher, Asylum Research) was also used to characterize the interfacial morphology of PDMS infiltrated membranes. To minimize the impact of roughness on the phase images, the cross sections were prepared using a Leica Microsystems cryo-ultramicrotome (model EMUC7 with EMFC7 sectioning system) equipped with an ultra–AFM MT16182 Diatome blade (feed: 100 nm, speed: 1 mm/s) at −140 °C. A cantilever (PPP-NCSTAuD, Nanosensors) with a force constant of 7.5 N/m and a resonance frequency of 157 kHz was used for all scans.

ATR-FTIR spectroscopy was performed at room temperature using an Agilent Cary 630 FTIR spectrometer equipped with a diamond crystal. Background spectra were acquired before each measurement. Measurements were conducted on the debonded PDMS surfaces to detect any membrane residuals. The characteristic C–F vibration bands were examined as signals for PVDF, while aromatic and sulfonic vibration bands were examined as signals for PES.

3. Results and discussion

3.1. Properties of the membranes and PDMS

Fig. 2 shows representative SEM images of both the surfaces and cross-sections of the V-650, S-U200 and S-U20 membranes. Note that V-100 possesses a symmetric pore structure similar to that of V-650 (SEM images are shown in Fig. S1). Likewise, S-M200 and S-M20 possess

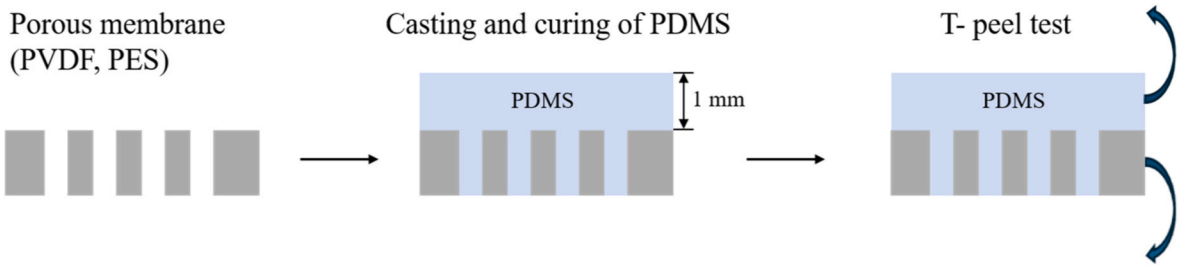

Fig. 1. Schematic illustration of membrane/PDMS adhesion sample preparation and testing.

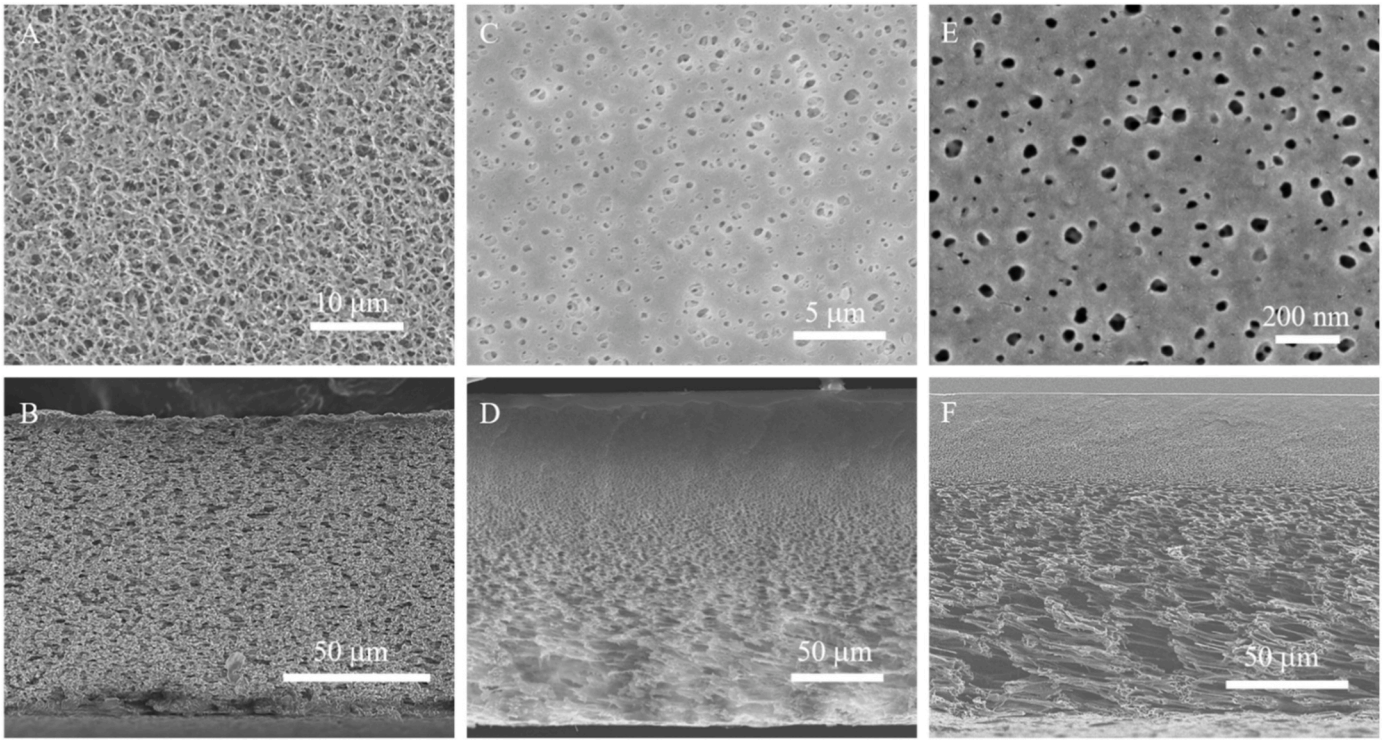

Fig. 2. SEM images of the membranes. (A) V-650 surface; (B) V-650 cross-section; (C) S-U200 surface; (D) S-U200 cross-section; (E) S-U20 surface; and (F) S-U20 cross-section.

nearly identical pore structures to S-U200 and S-U20, respectively, because the chemical modification does not alter the membrane morphology (SEM images of S-U20 are shown in Fig. S1). The characteristics of all membranes are listed in Table 1. The pore size rating was obtained by a standard particle retention method, the overall porosity was determined by mass/volume measurements, and the surface porosity was estimated from SEM images.

Fig. 3 shows the viscoelastic responses of pure PDMS at room temperature: (A) frequency dependence of the loss modulus $E''(\omega)$ and (B) tensile rate dependence of the fracture toughness ($G_{c,0}$). $G_{c,0}$ was estimated from $G_{c,0} = W_f h$, where W_f is the strain energy density at failure (estimated from the area under the stress-strain curve (inset of Fig. 3B) at a given strain rate) and h is the thickness of the PDMS (~1 mm). Note that the $G_{c,0}$ value obtained in such a way assumes that the entire PDMS thickness contributes elastic energy to the crack propagation, and therefore, represents the upper bound of the intrinsic fracture toughness of PDMS.

Both properties displayed similar frequency- and rate-dependent scaling behaviors. Specifically, $E'' \sim \omega^m$, with $m \approx 0.28$ ($R^2 = 0.99$), while $G_{c,0} \sim \dot{\varepsilon}^n$, with $n = 0.3$ ($R^2 = 0.92$). The physical origin of the similar scaling behavior between the linear viscoelastic response ($E''(\omega)$) and nonlinear fracture response ($G_{c,0}$) is unclear. Similar rate-dependence of fracture toughness has been reported for other elastomers [19,20], which is attributed to the viscoelastic dissipation during crack propagation. Although PDMS possesses a T_g of approximately −123 °C and the segmental relaxation rate is expected to be several orders of magnitude faster than the applied strain rates, a correlation nevertheless exists between dynamic modulus and fracture toughness. Similar correlations have also been observed in Johnson-Kendall-Roberts (JKR) - type adhesive contacts between PDMS and other substrates [21]. Nevertheless, $G_{c,0}$ values increase from approximately 200 N/m to approximately 1000 N/m with increasing strain rate. These values are consistent with a prior report, in which the fracture toughness of PDMS (Sylgard 184) was approximately 500 J/m^2 at a strain rate of 25 %/min [22], and fall within the range reported in the literature [23].

Table 1
Properties of all the membrane samples.

Membranes	Thickness (μm)	Nominal pore size (nm)	Overall porosity (%)	Surface porosity (%)
V-100	103	100	60	40
V-650	115	650	64	43
S-U200	175	200	80	18
S-M200	175	200	80	18
S-U20	140	20	73	10
S-M20	140	20	73	7.5

3.2. T-peel test results

Fig. 4A shows the unbonded region (manually separated PDMS layer and the membrane) and bonded region. A representative cross-sectional SEM image of PDMS-infiltrated V-650 is shown in Fig. 4B, confirming the complete pore-wetting by PDMS. The PDMS layer and membrane in the unbonded region were mounted onto the grips of the Instron (Fig. 4C) to conduct the T-peel test. Representative force-extension curves from the peel tests are shown in Fig. 4D. The interfacial fracture toughness, G_c, was calculated from the steady-state peel force (F_{peel}, the plateau on the force-extension curve), $G_c = 2F_{peel}/w$, where w is the width of the sample ($w = 12\ mm$).

Fig. 5 summarizes the G_c values for both PDMS/PVDF membranes (Fig. 5A) and PDMS/PES membranes (Fig. 5B). All membranes and dense films display increasing G_c values with increasing peel rate, with the power exponent ranging between 0.11 and 0.34, except S-M20 ($n = 0.59$), as listed in Table S1. The G_c values for PDMS/PVDF films increase from approximately 5 N/m to approximately 15 N/m with increasing peel rate, which are slightly larger than those of PDMS/PES films (approximately 2 -6 N/m). These G_c values are more than one order of magnitude larger than the values reported for PDMS adhesion with glass slides (approximately 0.2 J/m^2 from JKR-type contact

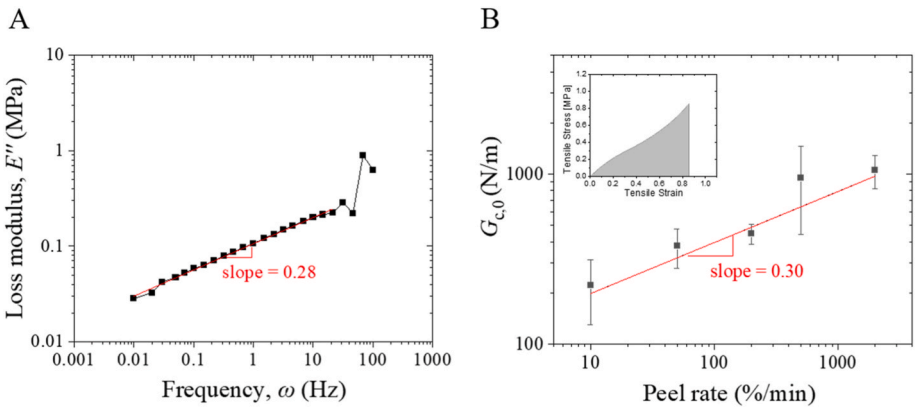

Fig. 3. (A) Loss modulus of PDMS as a function of frequency at room temperature, strain amplitude is 0.1 %. (B) Tensile fracture toughness ($G_{c,0}$) of PDMS as a function of peel rates. Inset shows a representative stress-strain curve from which the $G_{c,0}$ value was obtained (the shaded area under the curve). The error bars represent the standard deviation from averaging four replicates at each peel rate. The lines represent linear fit of the data with corresponding slopes labelled.

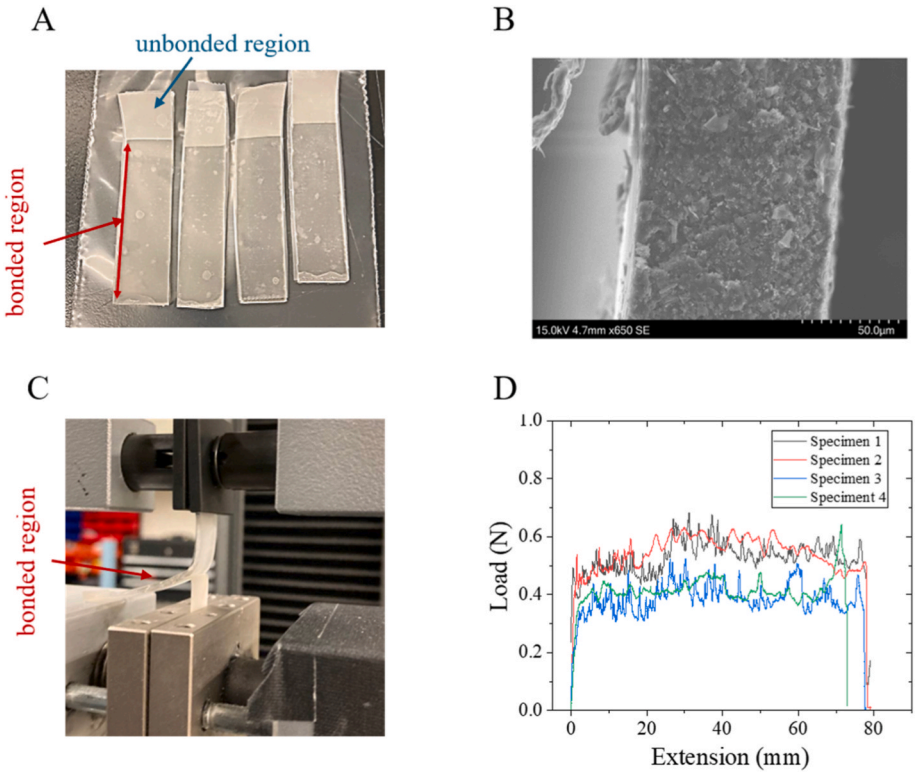

Fig. 4. T-Peel tests information. (A) Photo of PDMS/membrane samples showing the bonded and unbonded regions; (B) SEM image of the cross-section of PDMS/V-650 showing full infiltration of the pores; (C) Photo of one sample during T-peel test; (D) representative force-extension curves from the peel tests of four replicate samples (V-650, peel rate: 20 %/min), from which the interfacial fracture toughness was determined.

measurement) [24].

As mentioned earlier, adhesion between pre-cured PDMS film and PVDF (or PES) films was too small to determine using the T-peel tests (samples separated upon loading), consistent with the JKR-measurements. The higher G_c values obtained for the PDMS/PVDF films could be caused by the remaining roughness of the PVDF film (densified from the membranes). From AFM measurements (30 μm × 30 μm), the RMS roughness was 32.4 ± 18.9 nm for a similarly densified PES film. Such roughness would cause small degrees of PDMS interlocking for PDMS cured atop the PVDF and PES films but reduces the adhesion with pre-cured PDMS (elastic) by reducing contact area.

The G_c values for all membranes are significantly larger than those of the corresponding dense bilayers, but remain lower than the fracture toughness of pure PDMS. For the PES membranes with the same pore size, no significant differences were observed between the two different membrane chemistries ("U" vs "M"), indicating that mechanical interlocking is the main contributor to the interfacial fracture toughness.

Fig. 6 plots the ratios of interfacial fracture toughness as a function of nominal pore size for all the membranes, normalized by flat films ($G_{c,mem}/G_{c,film}$, Fig. 6A) or by fracture energy of PDMS (of $G_{c,mem}/G_{c,0}$, Fig. 6B). Note that both ratios show negligible dependency on peel rates (Fig. S2 and S3), and the values shown in Fig. 6 are averages across the different peel rates. For both PVDF membranes and PES membranes, the $G_{c,mem}/G_{c,film}$ ratio increases with increasing pore size: from approximately 5.7 (V-100) to approximately 12 (V-650), and from approximately 3 (S-U20) to approximately 27 (S-U200).

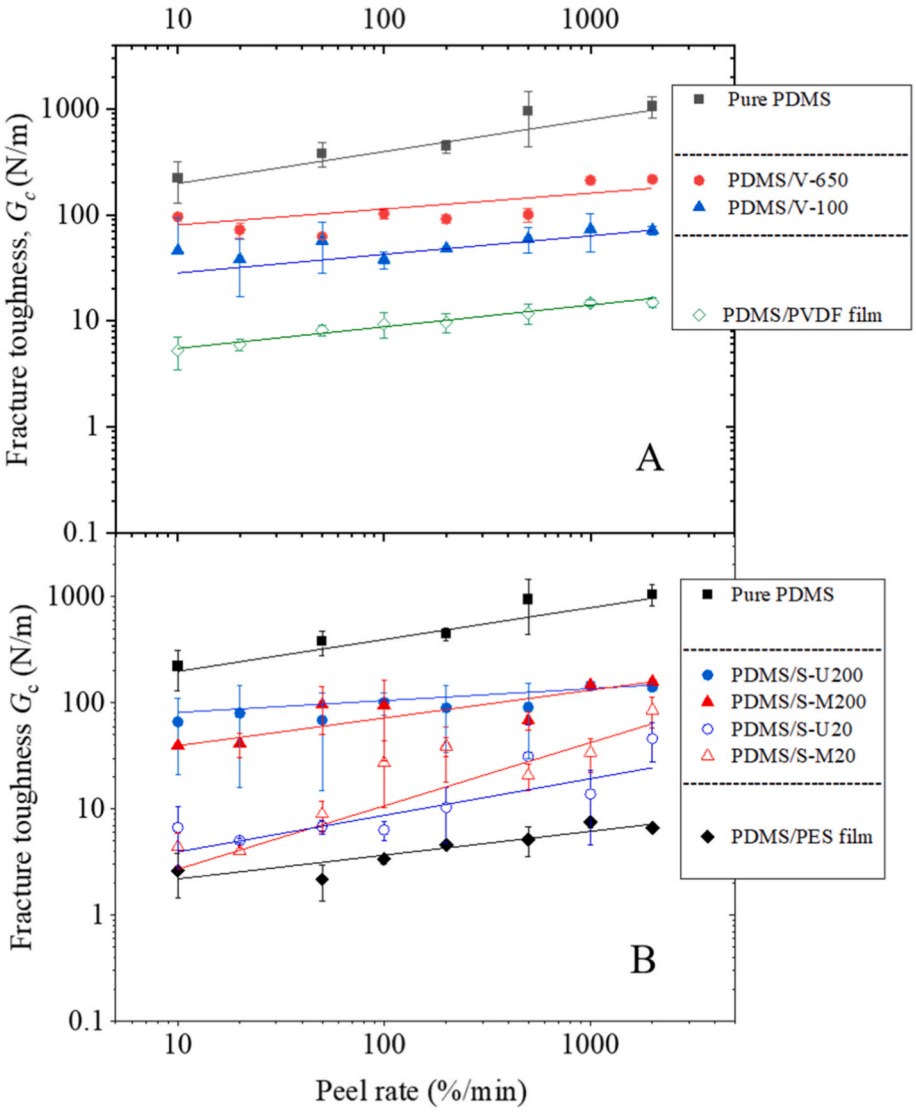

Fig. 5. Interfacial fracture toughness (G_c) as a function of peel rate for PDMS bonded with (A) two PVDF membranes (V-650 and V-100) and dense PVDF film, and (B) four PES membranes (S-U200, S-M200, S-U20, and S-M20) and dense PES film. Tensile fracture toughness of pure PDMS films ($G_{c,0}$) data is included in both plots.

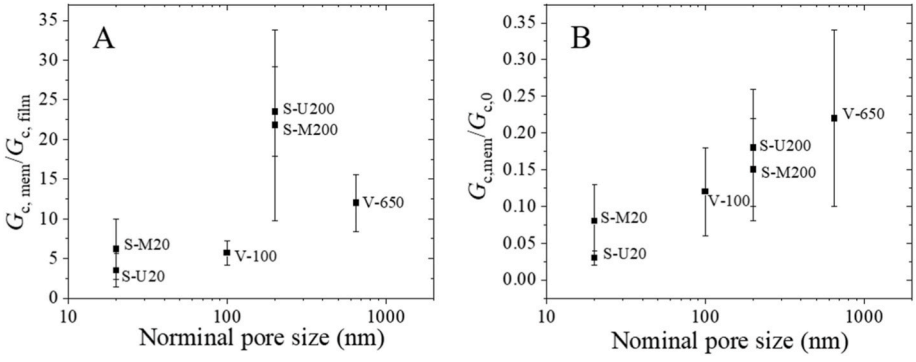

Fig. 6. Ratios of (A) $G_{c,mem}/G_{c,film}$ and (B) $G_{c,mem}/G_{c,0}$ for all six membranes. The ratios are average values of different peel rates, and the error bars correspond to the standard deviations.

Previous research has shown that hierarchical roughness can effectively enhance mechanical interlocking in epoxy resins [25]. In that study, 0.3-μm dendrites and high-angle pyramids led to adhesion enhancement of 1.5 % and 50 %, respectively, relative to flat surfaces. However, the combination of the two (0.3-μm dendrites on 2-μm high-angle pyramids) resulted in an adhesion enhancement of approximately 200 %. These results suggest that the membrane pore structures (Fig. 2) are even more effective in promoting mechanical interlocking than the above-mentioned surface features.

Interestingly, the $G_{c,mem}/G_{c,0}$ ratio correlates reasonably well with

the surface porosity of the asymmetric PES membranes, increasing from 3 %-7 % for the 20-nm membranes (S-U20 and S-M20) to 15 %-18 % for the 200-nm membranes (S-U200 and S-M200). In contrast, for the symmetric PVDF membranes, the $G_{c,mem}/G_{c,0}$ ratios (12 % - 22 %) are substantially lower than the surface porosity of both membranes (~40 %).

Adhesion of elastomers often exhibits weak power-law dependence (n = 0.1-0.3), due to viscoelastic dissipation during crack propagation [19]. All samples except S-M20 showed rate dependence within this range, indicating that the dissipation in PDMS dictates measured energy release rate. We attribute the slightly stronger rate dependence of S-M20 to the acrylamide coating on the membranes. Even though the same coating was used in S-M200, its impact is negligible due to the large pore size.

From SEM images of debonded surfaces, representative examples of which are shown in Fig. 7, interfacial failure appears to be the dominant debonding mechanism. ATR-FTIR analysis confirmed the absence of PVDF or PES residues on debonded PDMS surfaces (Fig. S4). Furthermore, nodules were observed across the PDMS surfaces, suggesting that fracture of the PDMS occurs near the top surfaces of the membranes. Collectively, these observations indicate that mechanical interlocking of PDMS within the membrane pores is the main contributor to the observed interfacial fracture toughness.

3.3. GENT model analysis

During peeling, cavitation occurs at the non-porous interface regions between PVDF (or PES) and PDMS, due to the low intrinsic thermodynamic adhesion between the two. This causes stress concentrations to be transferred to the infiltrated PDMS inside the membrane pores. Gent et al. analyzed the adhesion strength caused by mechanical interlocking of elastomers within arrays of cylindrical pores in metal plates [26]. The observed work of detachment of the infiltrated elastomers can be described by

$$G_a' = G_a\left(1 + 4\left(\frac{l}{a}\right)n\pi a^2\right) + lU_b n\pi a^2 \quad (1)$$

where G_a is the work of adhesion between two flat surfaces, l and a are the effective debonding length and diameter of the pores (from which the elastomer debonded), n is the number density of pores (number of pores per unit area); and U_b is the specific fracture energy of the elastomer (which can be adjusted by curing conditions).

Here, the fracture toughness obtained from the peel tests involves the same two contributions as the Gent model: intrinsic thermodynamic adhesion energy (the first term in Eq. (1)) and volumetric dissipation energy associated with PDMS fracture (the second term in Eq. (1)). By approximating the top layer of the membrane as an array of cylindrical pores, the interfacial fracture toughness can be analyzed using the Gent model. Based on Eq. (1), the fracture depth of PDMS within the membrane pores (l) can be calculated using the experimentally determined $G_{c,mem}$ (corresponding to the G_a' term in Eq. (1)) and $G_{c,film}$ (corresponding to the G_a term in Eq. (1)). The values of U_b for PDMS were calculated from the $G_{c,0}$ values shown in Fig. 3B. Fig. 8A summarizes the calculated values of l, averaged from different peel rates, as a function of pore size for all six membranes. Note that the surface porosity (Table 1) used to estimate the pore number density (n) may be underestimated because of the metal coating used for SEM imaging [27], which would lead to a slight overestimation of the calculated fracture depth (l).

The fracture of PDMS most likely occurs at the most constricted regions within the porous membranes. The effective fracture depth was estimated as approximately 100-200 nm below the membrane surfaces for S-U20 and V-100, but approximately 1-2 μm for S-U200 and V-650. Note that the pore size rating (e.g. 20 nm) of these membranes approximately corresponds to the smallest particle size that the membrane can reject. Given the broad distribution of pore sizes, the pore size rating often corresponds to the narrowest constriction, or "pore throats" within the membrane pore network [28].

Fig. 8B shows a representative cross-sectional atomic force microscopy (AFM) phase image of the PDMS/S-U200 interface, revealing regions where the PDMS is connected through narrow necks. It is therefore likely that fractures occur at these pore throats located nearest the membrane surface, as marked in the inset of Fig. 8B. Interestingly, the range of l values shown in Fig. 8A coincides with the typical "skin layer" thickness for asymmetric membranes (e.g. S-U20 and S-U200), as estimated from the flow path length based on Darcy's law [1,2,29,30]. Symmetric membranes such as V-100 and V-650 are generally not considered to possess distinct skin layers. Nevertheless, the results suggest the presence of similar near-surface pore constrictions that localize stress and ultimately govern PDMS fracture.

4. Conclusion

In summary, this study provides the first systematic examination of

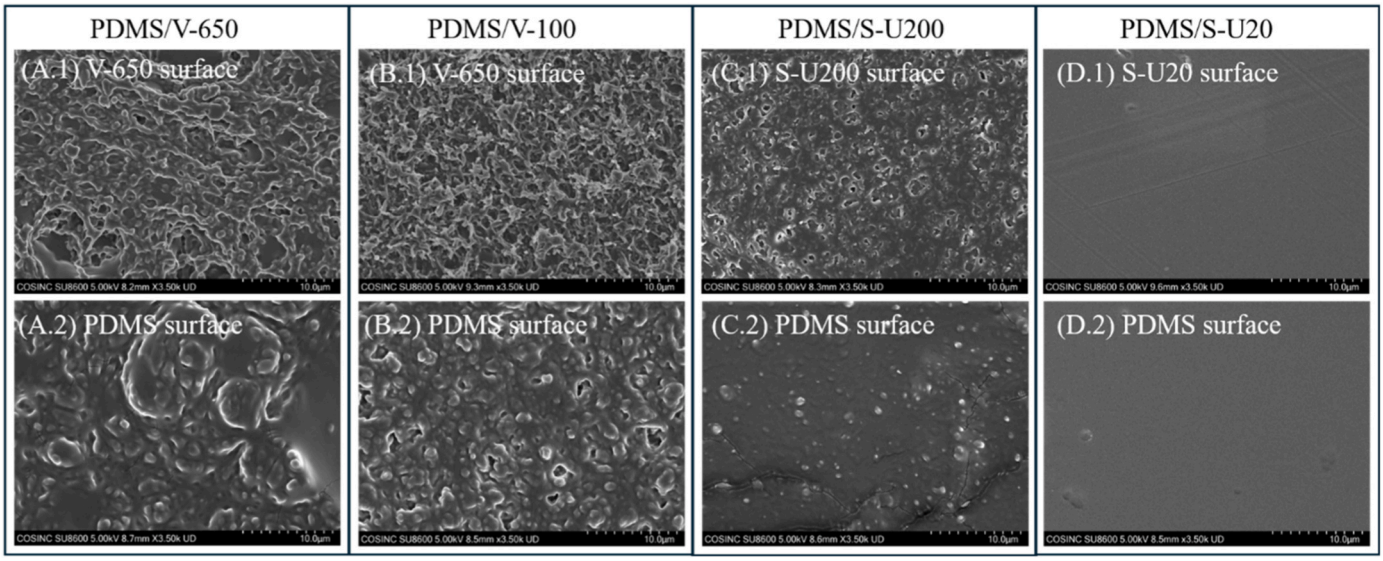

Fig. 7. Representative SEM images of debonded surfaces. (A.1) V-650, (B.1) V-100, (C.1) S-U200 and (D.1) S-U20. (A.2)-(D.2) are the corresponding PDMS surfaces. The peel rate was 50 %/min for PDMS-V100 and was 10 %/min for the remaining samples.

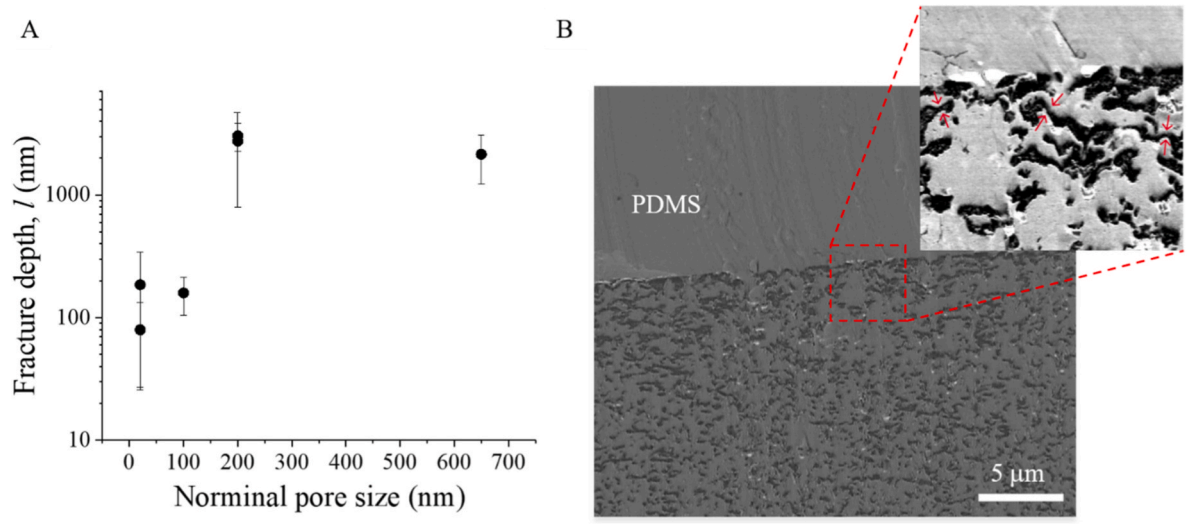

Fig. 8. Fracture depth analysis of infiltrated PDMS. (A) Fracture depth (l, calculated from Eq. (1)) as a function of nominal pore size ratings of the six membranes. (B) AFM phase image of cryomicrotomed PDMS/S-U200. The gray phase is PDMS and the darker phase is PES. The inset provides a high-resolution view of the boxed region, with arrows indicating potential pore throats.

adhesion behavior between infiltrated PDMS and porous membranes, including two symmetric PVDF membranes and four asymmetric PES membranes. All membranes displayed interfacial failure during the peel tests, and the corresponding interfacial fracture toughness, G_c, increased with peel rate. Compared with dense films, the porous membranes exhibited G_c values that were approximately 3 to 25 times higher, attributed to mechanical interlocking of the infiltrated PDMS. For each membrane type, the G_c value correlates well with pore size and porosity: larger pores or higher porosity lead to higher G_c values. Analysis using the Gent model suggests that PDMS fracture occurs in the pore throats near the membrane surfaces, approximately 100 - 200 nm below the surface for membranes with pore-size ratings at or below 100 nm, and approximately 1 - 2 µm for membranes with pore-size ratings at or above 200 nm.

These findings provide fundamental insights into the interfacial interactions between PDMS (and potentially other elastomers) and porous supports and can guide the design and manufacturing of membrane devices. For applications involving relatively thick PDMS selective layers (e.g., several micrometers or thicker), infiltration beyond the fracture depth does not further enhance adhesion, but instead increases transport resistance. Therefore, excess infiltration should be avoided to maintain high membrane permeance. In contrast, for applications employing ultrathin PDMS selective layers (e.g., on the order of hundreds of nanometers), the corresponding infiltration depth is much smaller, resulting in lower interfacial adhesion than the values reported in this work, as predicted by the Gent model. Unfortunately, conventional peel tests are not sufficiently sensitive to quantify the adhesion strength of such ultrathin systems. Alternative techniques, such as blister tests, are therefore required.

CRediT authorship contribution statement

Meril Moni: Data curation, Formal analysis, Methodology, Writing – review & editing. **Emma Letourneau:** Data curation, Formal analysis, Writing – review & editing. **Sundus Imtiaz Qureshi:** Formal analysis, Writing – review & editing. **Christina Carbrello:** Conceptualization, Funding acquisition, Writing – review & editing. **Jason Killgore:** Data curation, Formal analysis, Writing – review & editing. **Yifu Ding:** Conceptualization, Formal analysis, Funding acquisition, Methodology, Project administration, Supervision, Writing – original draft.

Declaration of competing interests

The authors declare that they have no known competing financial interests or personal relationships that could have appeared to influence the work reported in this paper.

Acknowledgment

The authors appreciate the research support of the National Science Foundation (NSF) Industry/University Cooperative Research Center for Membrane Application Science and Technology (MAST) Center at the University of Colorado Boulder (UCB, EEC 2310937). We also acknowledge support from the Desalination and Water Purification Research (DWPR) Program of the U.S. Bureau of Reclamation (Award number R23AC00436). Certain equipment, instruments, software, or materials are identified in this paper in order to specify the experimental procedure adequately. Such identification is not intended to imply recommendation or endorsement of any product or service by NIST, nor is it intended to imply that the materials or equipment identified are necessarily the best available for the purpose.

Appendix A. Supplementary data

Supplementary data to this article can be found online at https://doi.org/10.1016/j.memsci.2026.126018.

Data availability

Data will be made available on request.

References

[1] M. Mulder, Basic Principles of Membrane Technology, second ed., Kluwer Academic, Dordrecht ; Boston, 1996.
[2] R.W. Baker, Membrane Technology and Applications, vol. 3, Wiley, Chichester, West Sussex, 2012.
[3] G. Liu, W. Jin, Pervaporation membrane materials: recent trends and perspectives, J. Membr. Sci. 636 (2021) 119557, https://doi.org/10.1016/j.memsci.2021.119557.
[4] L. Li, Z. Xiao, S. Tan, L. Pu, Z. Zhang, Composite PDMS membrane with high flux for the separation of organics from water by pervaporation, J. Membr. Sci. 243 (1) (2004) 177–187, https://doi.org/10.1016/j.memsci.2004.06.015.
[5] L.-F. Ren, C. Liu, Y. Xu, X. Zhang, J. Shao, Y. He, High-performance electrospinning-phase inversion composite PDMS membrane for extractive membrane bioreactor: fabrication, characterization, optimization and application,

J. Membr. Sci. 597 (2020) 117624, https://doi.org/10.1016/j.memsci.2019.117624.
[6] G. Zhang, H. Lin, Indispensable gutter layers in thin-film composite membranes for carbon capture, Green Energy Environ. 9 (8) (2024) 1220–1238, https://doi.org/10.1016/j.gee.2023.08.001.
[7] G. Zhang, T.N. Tran, L. Huang, E. Deng, A. Blevins, W. Guo, Y. Ding, H. Lin, Thin-film composite membranes based on hyperbranched Poly(Ethylene oxide) for CO2/N2 separation, J. Membr. Sci. 644 (2022) 120184, https://doi.org/10.1016/j.memsci.2021.120184.
[8] T.C. Merkel, V.I. Bondar, K. Nagai, B.D. Freeman, I. Pinnau, Gas sorption, diffusion, and permeation in Poly(Dimethylsiloxane), J. Polym. Sci., Part B: Polym. Phys. 38 (3) (2000) 415–434, https://doi.org/10.1002/(SICI)1099-0488(20000201)38:3%3C415::AID-POLB8%3E3.0.CO;2-Z.
[9] G. Genduso, A. Missinne, Z. Ali, W. Ogieglo, B. Van der Bruggen, I. Pinnau, Hydrophobic polydimethylsiloxane thin-film composite membranes for the efficient pervaporative desalination of seawater and brines, Sep. Purif. Technol. 280 (2022) 119819, https://doi.org/10.1016/j.seppur.2021.119819.
[10] L. Zhu, L. Huang, S.R. Venna, A.K. Blevins, Y. Ding, D.P. Hopkinson, M.T. Swihart, H. Lin, Scalable polymeric few-nanometer organosilica membranes with hydrothermal stability for selective hydrogen separation, ACS Nano 15 (7) (2021) 12119–12128, https://doi.org/10.1021/acsnano.1c03492.
[11] M. Wang, S.K. Ghosh, C.M. Stafford, A.K. Blevins, S. Huang, J. Martinez, R. Long, C.N. Bowman, J.P. Killgore, M. Zou, Y. Ding, Snakeskin-inspired elastomers with extremely low coefficient of friction under dry conditions, ACS Appl. Mater. Interfaces 12 (51) (2020) 57450–57460, https://doi.org/10.1021/acsami.0c18316.
[12] Y. Pan, Y. Hang, X. Zhao, G. Liu, W. Jin, Optimizing separation performance and interfacial adhesion of PDMS/PVDF composite membranes for butanol recovery from aqueous solution, J. Membr. Sci. 579 (2019) 210–218, https://doi.org/10.1016/j.memsci.2019.03.008.
[13] Y. Hang, G. Liu, K. Huang, W. Jin, Mechanical properties and interfacial adhesion of composite membranes probed by in-situ nano-Indentation/Scratch technique, J. Membr. Sci. 494 (2015) 205–215, https://doi.org/10.1016/j.memsci.2015.05.076.
[14] R. Jain, C. Carbrello, K. Youngbear, S. Foley, R. Long, Y. Ding, Enhancing membrane adhesion to polymeric substrates via plasma treatment, ACS Appl. Polym. Mater. (2026), https://doi.org/10.1021/acsapm.5c04051.
[15] J. Martinez, M. Aghajani, Y. Lu, A.K. Blevins, S. Fan, M. Wang, J.P. Killgore, S. B. Perez, J. Patel, C. Carbrello, S. Foley, R. Sylvia, R. Long, R. Castro, Y. Ding, Capillary bonding of membranes by viscous polymers: infiltration kinetics and mechanical integrity of the bonded polymer/membrane structures, J. Membr. Sci. 641 (2022) 119898, https://doi.org/10.1016/j.memsci.2021.119898.
[16] J. Martinez, S. Fan, S. Rabade, A.K. Blevins, K. Fung, J.P. Killgore, S.B. Perez, K. Youngbear, C. Carbrello, S. Foley, X. Ding, R. Long, R. Castro, Y. Ding, Capillary infiltration kinetics in highly asymmetric porous membranes and the resulting debonding behaviors, Polymer 263 (2022) 125529, https://doi.org/10.1016/j.polymer.2022.125529.
[17] R. Jain, J. Martinez, R. Lovison, K. Fung, J.P. Killgore, C. Carbrello, K. Youngbear, S. Foley, R. Long, Y. Ding, Thermomechanical bonding between asymmetric porous membranes and polymers, J. Membr. Sci. 723 (2025) 123931, https://doi.org/10.1016/j.memsci.2025.123931.
[18] R. Lovison, H. Kabutz, E. Letourneau, K. Fung, R. Jain, C.M. Carbrello, K. Jayaram, Y. Ding, Femtosecond laser ablation of porous PVDF and PES membranes: ablation behaviors and In-Plane cross-sectioning, J. Polym. Sci. 63 (17) (2025) 3578–3590, https://doi.org/10.1002/pol.20250427.
[19] A.N. Gent, Adhesion and strength of viscoelastic solids. Is there a relationship between adhesion and bulk properties? Langmuir 12 (19) (1996) 4492–4496, https://doi.org/10.1021/la950887q.
[20] P.G. de Gennes, Soft adhesives, Langmuir 12 (19) (1996) 4497–4500, https://doi.org/10.1021/la950886y.
[21] K.R. VanDonselaar, D.A. Bellido-Aguilar, M. Safaripour, H. Kim, J.J. Watkins, A. J. Crosby, D.C. Webster, A.B. Croll, Silicone elastomers and the persson-brener adhesion model, J. Chem. Phys. 159 (18) (2023) 184708, https://doi.org/10.1063/5.0172415.
[22] Y. Tao, S. Mei, H. Yi, X. Pan, R. Zhang, Z. Li, Enhancing fracture toughness of polydimethylsiloxane with cyclosiloxane hybrid polymer microspheres, Compos. Sci. Technol. 244 (2023) 110314, https://doi.org/10.1016/j.compscitech.2023.110314.
[23] Z. Wang, C. Xiang, X. Yao, P. Le Floch, J. Mendez, Z. Suo, Stretchable materials of high toughness and low hysteresis, Proc. Natl. Acad. Sci. 116 (13) (2019) 5967–5972, https://doi.org/10.1073/pnas.1821420116.
[24] T. Thomas, A.J. Crosby, Controlling adhesion with surface hole patterns, J. Adhes. 82 (3) (2006) 311–329, https://doi.org/10.1080/00218460600646610.
[25] D.J. Arrowsmith, Adhesion of electroformed copper and nickel to plastic laminates, Trans. IMF 48 (1) (1970) 88–92, https://doi.org/10.1080/00202967.1970.11870136.
[26] A.N. Gent, C.-W. Lin, Model studies of the effect of surface roughness and mechanical interlocking on adhesion, J. Adhes. 32 (2–3) (1990) 113–125, https://doi.org/10.1080/00218469008030185.
[27] S. Zeinali Danalou, D. Yu, N.R. Sarker, H. Chamani, J.Y. Howe, P.C. Lee, J. R. Werber, From coated to uncoated: scanning electron microscopy corrections to estimate the true surface pore size in nanoporous membranes, ACS Appl. Mater. Interfaces 17 (46) (2025) 63804–63816, https://doi.org/10.1021/acsami.5c17764.
[28] K.P. Brickey, A.L. Zydney, E.D. Gomez, FIB-SEM tomography reveals the nanoscale 3D morphology of virus removal filters, J. Membr. Sci. 640 (2021) 119766, https://doi.org/10.1016/j.memsci.2021.119766.
[29] H. Strathmann, K. Kock, P. Amar, R.W. Baker, The formation mechanism of asymmetric membranes, Desalination 16 (2) (1975) 179–203, https://doi.org/10.1016/S0011-9164(00)82092-5.
[30] R. Lovison, M.A. Afzal, C.M. Carbrello, A.L. Zydney, Y. Ding, Fractal analysis of porous structure and permeability of separation membranes, J. Membr. Sci. 730 (2025) 124168, https://doi.org/10.1016/j.memsci.2025.124168.